RESEARCH ARTICLE
SOLID EARTH: SEISMOLOGY

Earth and Planetary Physics
9: 1048–1060, 2025
doi: 10.26464/epp2025053

Joint inversion of body wave arrival times and surface wave dispersion data for the subduction zone velocity structure of central Chile

ZiXin Chen[1], HaiJiang Zhang[1,2*], Lei Gao[1,3], Ying Liu[1], ShaoBo Yang[1,4], and Diana Comte[5]

[1]School of Earth and Space Sciences, University of Science and Technology of China, Hefei 230026, China;

[2]State Key Laboratory of Precision Geodesy, University of Science and Technology of China, Hefei 230026, China;

[3]China Deep Exploration Center, Chinese Academy of Geological Sciences, Beijing 100037, China;

[4]School of Carbon Neutrality Science and Engineering, Anhui University of Science and Technology, Hefei 231131, China;

[5]Departamento de Geofísica, Advanced Mining Technology Center, Facultad de Ciencias Físicas y Matemáticas, Universidad de Chile, Blanco Encalada, 2002, Santiago, Chile

Key Points:

- Joint inversion of body wave arrival times and surface wave phase velocity maps is used to determine the velocity structure of the central Chile subduction zone.
- The velocity model reveals an eastward-dipping high-velocity slab of 40–50 km thick, with a low-velocity layer beneath it.
- The widespread low-velocity anomalies in the crust are imaged beneath the Central Volcanic Zone of the Andes, representing crustal magma chambers for various volcanoes.

Citation: Chen, Z. X., Zhang, H. J., Gao, L., Liu, Y., Yang, S. B., and Comte, D. (2025). Joint inversion of body wave arrival times and surface wave dispersion data for the subduction zone velocity structure of central Chile. *Earth Planet. Phys.*, *9*(5), 1048–1060. http://doi.org/10.26464/epp2025053

Abstract: The Chilean Pampean flat slab subduction segment is characterized by the nearly horizontal subduction of the Nazca Plate within the depth range of 100–120 km. Numerous seismic tomography studies have been conducted to investigate its velocity structure; however, they have used only seismic body wave data or surface wave data. As a result, the existing velocity models in the region may have relatively large uncertainties. In this study, we use body wave arrival times from earthquakes occurring in central Chile between 2014 and 2019, as well as Rayleigh wave phase velocity maps at periods of 5–80 s from ambient noise empirical Green's functions in Chile. By jointly using body wave arrival times and surface wave dispersion data, we refine the V_S model and improve earthquake locations in the central Chile subduction zone. Compared with previous velocity models, our velocity model better reveals an eastward-dipping high-velocity plate representing the subducting Nazca Plate, which is 40–50 km thick and is more consistent with the slab thickness estimated by receiver function imaging and thermal modeling. Overall, the intraslab seismicity distribution spatially correlates well with the slab high-velocity anomalies except along the subduction paths of the Copiapó Ridge and Juan Fernández Ridge. Additionally, parallel low-velocity stripes are imaged beneath the subducting plate, which are likely associated with the accumulated melts. The joint inversion velocity model also resolves widespread low-velocity anomalies in the crust beneath the Central Volcanic Zone of the central Andes, likely representing crustal magma chambers for various volcanoes.

Keywords: Chilean Pampean flat slab; seismic joint inversion; seismic velocity model; Central Volcanic Zone of the central Andes; Copiapó Ridge; Juan Fernández Ridge

1. Introduction

The Nazca–South American subduction zone, extending more than 7000 km from north to south, is one of the longest subduction zones in the world, and the morphology of the subducting plate exhibits substantial temporal and spatial variations (Ramos and Folguera, 2009). Currently, three prominent flat slab segments are identified beneath South America: the Bucaramanga flat slab segment in Colombia, the Peruvian flat slab segment in Peru, and the Pampean flat slab segment in central Chile (Marot et al., 2014). The flat subduction can influence volcanic activity in the overriding plate, the coupling state along the subducting plate interface, and the deformation of both plates. It is generally believed that the two gaps in the Quaternary volcanic arc of the Andes correspond to the Peruvian flat subduction zone and the Pampean flat

First author: Z. X. Chen, chenzx23@mail.ustc.edu.cn
Correspondence to: H. J. Zhang, zhang11@ustc.edu.cn
Received 16 JAN 2025; Accepted 02 APR 2025.
First Published online 09 JUN 2025.

subduction zone, respectively (Barazangi and Isacks, 1976; Kopp et al., 2004; Ramos and Folguera, 2009). Several mechanisms have been proposed for the formation of flat slab subduction, including the trenchward motion of the overriding plate, the suction between overriding and subducting plates, elevated subduction velocity, and the subduction of oceanic ridges and plateaus (Cross and Pilger, 1982; Gutscher et al., 2000; Manea et al., 2012; O' Driscoll et al., 2012; Haddon and Porter, 2018). Among these, the subduction of the thick oceanic ridges is well documented in the Bucaramanga, Peruvian, and Pampean flat slab segments (Pilger, 1981; Gutscher et al., 2000; Ramos and Folguera, 2009; Portner et al., 2017).

The Pampean flat subduction zone spans ~28°S and ~32°S, where the Nazca Plate subducts toward the South American Plate at a rate of approximately 6.7 cm/yr (Angermann et al., 1999; DeMets et al., 2010). The flat subduction occurs in the depth range of 100–120 km, and then the slab continues to subduct normally at an angle of approximately 30°. Previous studies have suggested that the Pampean flat subduction is associated with subduction of the relatively young plate (35–40 Ma) and hydrated lithosphere (Kopp et al., 2004), as well as the Juan Fernández Ridge (JFR). The JFR, located near 32.5°S, represents the most prominent oceanic feature in the offshore area, as shown in Figure 1a (Contreras-Reyes and Carrizo, 2011). This ridge was formed away from the spreading center and is composed of a series of narrow hotspot chains (Pilger, 1981; von Huene et al., 1997; Bello-González et al., 2018). It has migrated southward over time: around 40–20 Ma, it subducted beneath the Altiplano and Puna Plateaus, and by approximately 12–8 Ma, it had subducted beneath the southern Puna Plateau (Yáñez et al., 2001; Bello-González et al., 2018). In addition, a recent study has suggested that the Copiapó Ridge plays an important role in causing the flat slab subduction (Gao L et al., 2025).

Many studies have focused on imaging the structures of the flat slab and overriding plate of the Pampean flat subduction zone by using various seismic methods (Wagner et al., 2005, 2006; Gans et al., 2011; Ward et al., 2013, 2017; Marot et al., 2014; Portner et al., 2017, 2020; Haddon and Porter, 2018; Gao YJ et al., 2021a, b; Liu M and Gao HY, 2022; Navarro-Aránguiz et al., 2022; Gao L et al., 2025). The receiver function results indicate that the Moho beneath the main Cordillera is approximately 70 km deep, whereas the oceanic crust thickening caused by JFR subduction is approximately 15–20 km deep (Gans et al., 2011; Haddon and Porter, 2018). Regional-scale seismic tomography results reveal velocity features related to the transition from normal to flat subduction, as well as corresponding variations in water content (Wagner et al., 2005, 2006; Marot et al., 2014; Gao L et al., 2025). Various hypotheses have been proposed regarding how the subducting plate transits from normal to flat subduction (Portner et al., 2017, 2020; Gao YJ et al., 2021b; Liu M and Gao HY, 2022; Gao L et al., 2025). However, the existing seismic tomography studies have used only one type of seismic data, and the existing models can be further improved over the inherent limitation of using a single type of seismic data to invert for the velocity models. For example, body wave seismic tomography can resolve the model region well only where ray path coverage is good; thus, it generally has poor resolution at shallow depths. In comparison, surface wave tomography with dispersion data at short periods can resolve shallow depths well, but it generally has poor resolution at greater depths.

Joint inversion of different seismic data types has been shown to

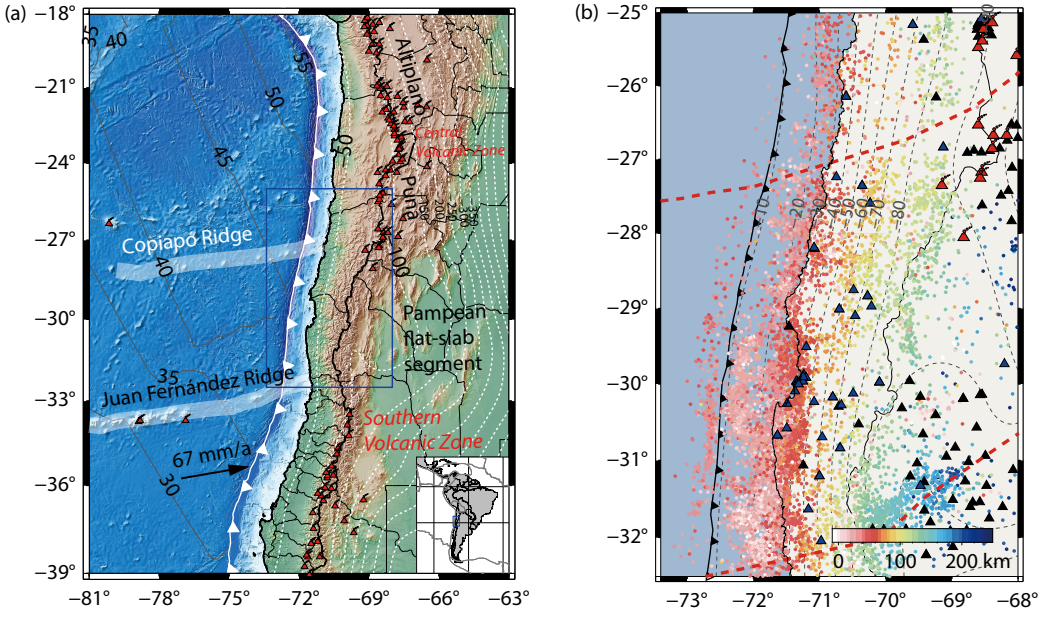

Figure 1. (a) Geological settings of the central Andes and the oceanic Nazca Plate. The blue box marks our study area. Thick white lines denote the Copiapó Ridge and Juan Fernández Ridge. (b) Distribution of stations and earthquakes in the study area (blue box in panel [a]). The colored dots represent the relocated earthquakes, the red volcanic symbols represent volcanoes, the blue triangles represent seismic stations with body wave arrival times, and the black triangles represent the stations with surface wave data. The dashed red lines represent predicted paths for the Copiapó Ridge and Juan Fernández Ridge tracks (Bello-González et al., 2018).

better constrain velocity models across different scales because of their complementary strengths (Zhang HJ et al., 2014; Fang HJ et al., 2016; Syracuse et al., 2016, 2017; Golos et al., 2018; Han SC et al., 2022). For example, Comte et al. (2016) conducted a joint inversion of body wave and surface wave data in northern Chile and determined more detailed V_P, V_S, and V_P/V_S models. For this reason, in this study we assemble body wave arrival times and surface wave dispersion data in central Chile and conduct a joint inversion of both data types. The complementary strengths of these two data types allow for improved constraints on the velocity structures of the subducting slab and overriding plate.

2. Data and Method

2.1 Body Wave Arrival Times

In this study, we collect seismic waveforms for 15,087 earthquakes recorded by 40 broadband seismometers between 2014 and 2019 from the Chilean Centro Sismológico Nacional (CSN), the Integrated Plate boundary Observatory Chile (IPOC) seismic network, and the GeoForschungsZentrum (GFZ) deployments in Chile. We use the same data processing procedure as described in Gao L et al. (2025) to pick first *P*- and *S*-wave arrivals. Figure S1 shows an example of picking *P*- and *S*-wave arrival times on waveforms for one event. In total, 213,961 *P*-wave arrival times and 182,519 *S*-wave arrival times were obtained.

To determine the initial earthquake locations, we utilize the NonLinLoc method (Lomax et al., 2000). Considering the strong lateral velocity heterogeneity in the study area, we calculate the travel-time tables for each station by using the three-dimensional (3D) V_P and V_S models determined by full waveform seismic inversion (Gao YJ et al., 2021a, b) and the spherical Earth finite difference travel-time calculation method (Zhang HJ et al., 2012). In this way, we can fully take into account the spherical shape of the Earth and the 3D velocity variations in the study region, enabling more accurate earthquake locations.

For earthquake locations from the NonLinLoc method, we retain only those with location uncertainties smaller than 10 km in all three directions. We further select the arrival times according to the epicentral travel-time curves by removing outliers from the main trend (Figure 2). Finally, we obtain 138,994 *P*-wave arrival times and 97,459 *S*-wave arrival times for 9467 earthquakes. In addition, we construct differential arrival times for event pairs with epicentral distances between 10 and 100 km, requiring each pair to have at least 6 common observations. A total of 19,721,451 *P*-wave and 11,163,885 *S*-wave differential arrival times are also constructed from absolute times, with an average event spacing of 18.6 km.

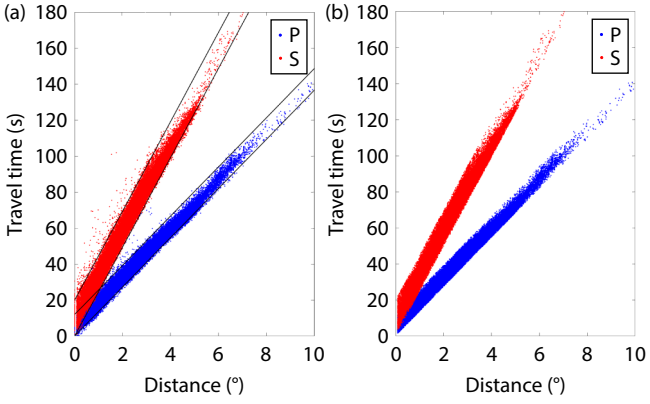

Figure 2. (a) Travel-time curves of all *P*- and *S*-wave data. The blue and red dots represent the *P*- and *S*-wave travel times, respectively. The straight black lines are used to select the data. (b) Travel-time curves of *P*- and *S*-wave data after selection.

2.2 Surface Wave Phase Velocity Maps

For surface wave data, we collect the empirical Green's functions (EGFs) extracted from continuous ambient noise data for the Chilean region by Liu M and Gao HY (2022). Their study uses ambient noise records for 460 broadband stations across Chile between 1994 and 2019, with 121 stations located within the study area (Figure 1b). The EGFs of the station pairs show clear Rayleigh wave signals at periods ranging from 5 to 80 s (Figure S2).

We adopt the deep learning-based DisperPicker method to automatically extract surface wave phase velocity dispersion curves (Yang SB et al., 2022). Figure 3b shows examples of the phase velocity dispersion curve extraction when using the DisperPicker method for two station pairs. A total of 8497 phase velocity dispersion curves between station pairs are extracted for the period of 5 to 80 s. Subsequently, to ensure the quality of the dispersion curves, we apply a bunching analysis to select the data by removing dispersion curves with similar paths and those with standard deviations greater than twice the mean. Finally, 6505 phase velocity dispersion curves are obtained (Figure S3).

Subsequently, we invert the two-dimensional (2D) phase velocity maps at different periods by using the fast-marching surface tomography method (FMST; Rawlinson and Sambridge, 2003, 2005). The ray paths exhibit adequate coverage across all periods (Figure S4). To maximize the utilization of available EGFs constructed by Liu M and Gao HY (2022), the 2D phase velocity inversion is performed over the entire station distribution area.

To evaluate the resolving ability of the available station-pair surface wave dispersion data, we first perform a checkerboard resolution test. For each period, we construct a 2D checkerboard model with a grid size of 0.4° × 1.0° in longitude and latitude, with velocity anomalies of ±0.5 km/s on alternative grid nodes with respect to a constant velocity. The recovered checkerboard models at different periods are shown in Figure 4. The recovered checkerboard model with finer grid intervals of 0.2° × 0.5° in longitude and latitude also shows good recovery in the study area (Figure S5).

For the 2D phase velocity inversion, we use the inversion grid with intervals of 0.2° × 0.5° in latitude and longitude as the second checkerboard resolution test (Figure S5). The optimal damping and smoothing parameters are selected via a trade-off analysis, both of which are 30 (Figure S6a, b). After 6 iterations, the surface wave travel-time residuals become more concentrated around 0 s compared with the initial residuals (Figure S6c), with the root mean square (RMS) travel-time residuals decreasing from 7.78 to

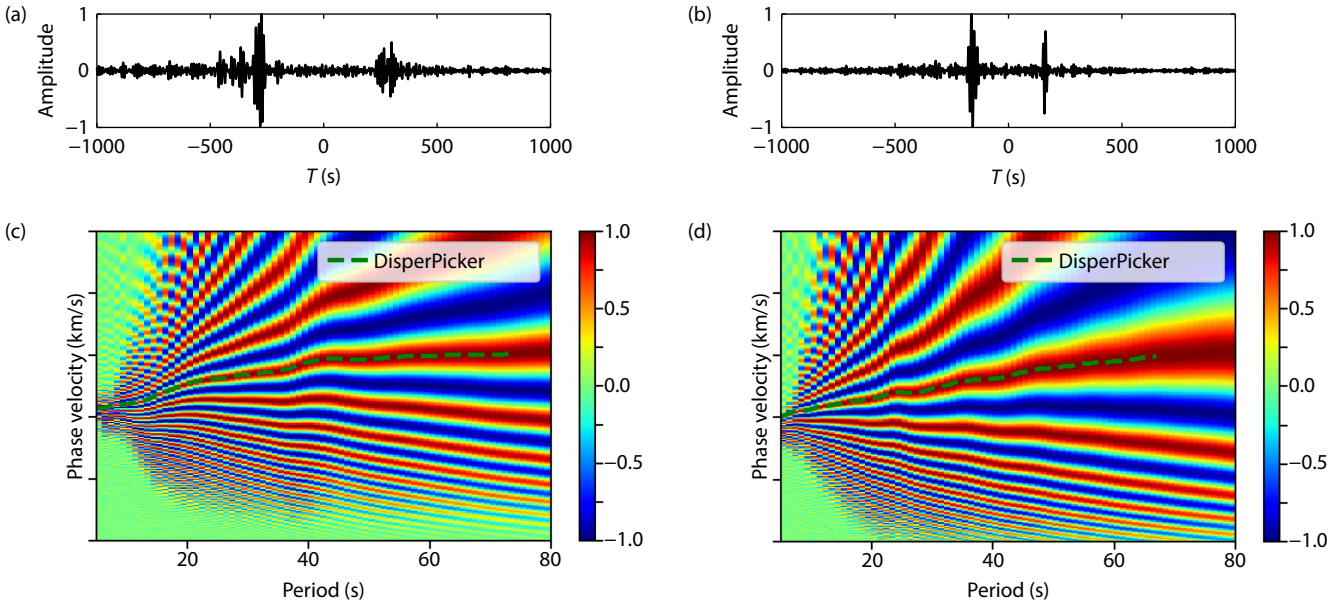

Figure 3. Examples of EGF and phase velocity dispersion curve picking by the DisperPicker method. (a) EGF for station pair PB04 and CORT in the 20–80 s period. The horizontal axis represents time in second, while the vertical axis represents the normalized amplitude. (b) EGF for station pair PB06 and EW18 in the 20–80 s period. (c) Phase velocity dispersion curve (dashed line) extracted for the EGF in (a). (d) Phase velocity dispersion curve (dashed line) extracted for the EGF in (b).

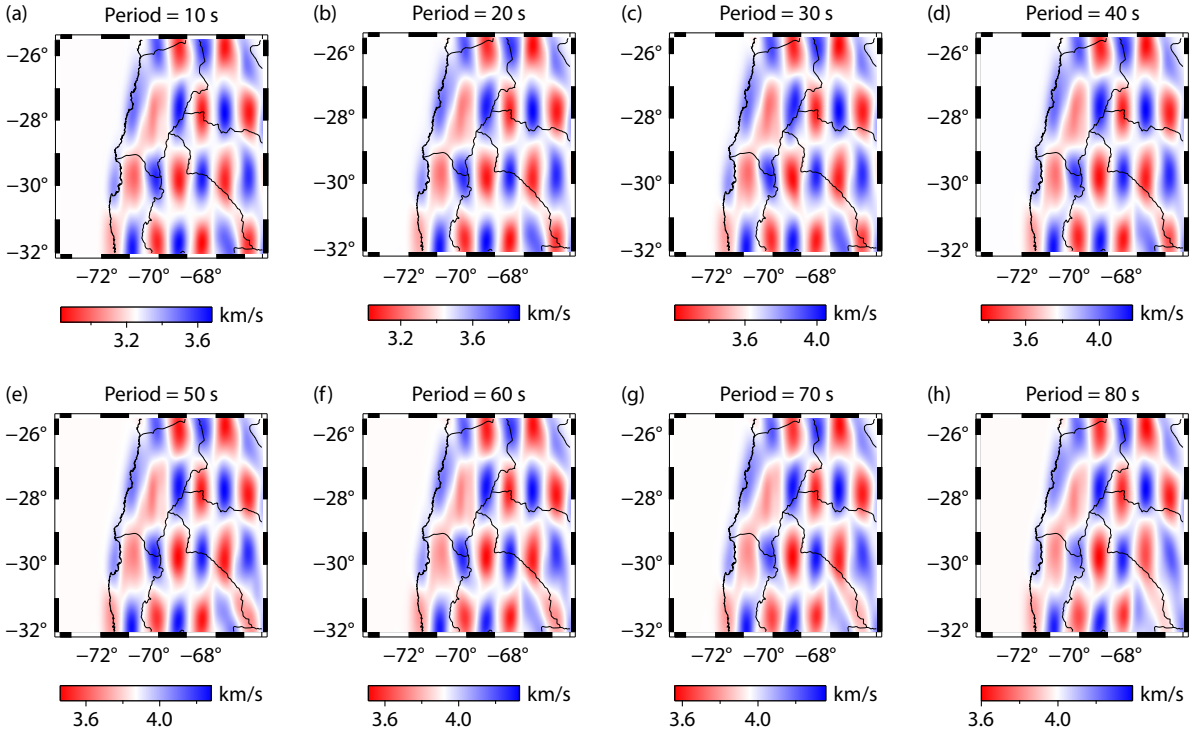

Figure 4. Recovered checkerboard patterns for phase velocity maps at different periods for the central Chile subduction zone. (a) 10 s, (b) 20 s, (c) 30 s, (d) 40 s, (e) 50 s, (f) 60 s, (g) 70 s, and (h) 80 s.

5.38 s after the inversion. Figure 5 shows the inverted phase velocity maps at different periods. Overall, these maps are consistent with the subducting features in this region. For example, high-velocity anomalies, which represent the subducting Nazca Plate, shift eastward from the western side as the period increases. In the northeastern part of the study area, low-velocity anomalies are widely distributed, which likely indicate partial melting from the crust to the mantle wedge beneath the volcanic arc region.

2.3 Joint Inversion Methodology

Here, we adopt the joint inversion algorithm of Zhang HJ et al. (2014) and Han SC et al. (2022) to jointly use body wave arrival

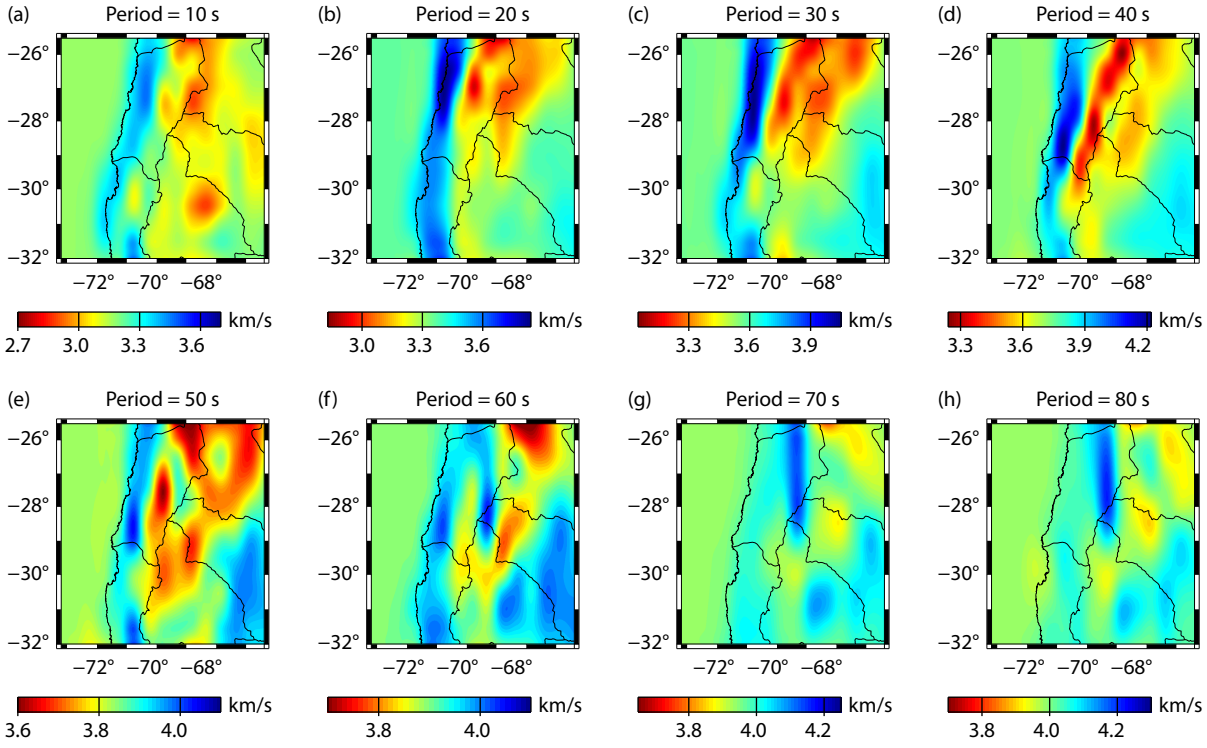

Figure 5. The inverted phase velocity maps at different periods. (a) 10 s, (b) 20 s, (c) 30 s, (d) 40 s, (e) 50 s, (f) 60 s, (g) 70 s, and (h) 80 s.

times and surface wave phase (or group) velocity maps to simultaneously determine V_P, V_S, and earthquake locations. In this method, body wave P and S arrival times are used to invert for source parameters as well as V_P and V_S models, whereas surface wave data are used only to constrain the V_S model. Therefore, compared with separate inversions using either body wave arrival times or surface wave dispersion data, this joint inversion algorithm can better constrain the V_S model.

The body wave inversion part is based on the regional-scale double difference (DD) tomography method (Zhang HJ and Thurber, 2003). The surface wave inversion part is based on the inversion scheme proposed by Maceira and Ammon (2009), which uses the DISPER80 algorithm (Saito, 1988) to calculate the dispersion curve with a layer model. The joint inversion system is represented as follows:

$$\begin{bmatrix} \mu_1 \boldsymbol{G}_H^{T_P} & \mu_1 \boldsymbol{G}_{V_P}^{T_P} & 0 \\ \mu_2 \boldsymbol{G}_H^{T_S} & 0 & \mu_2 \boldsymbol{G}_{V_S}^{T_S} \\ 0 & 0 & \mu_3 \boldsymbol{G}_{V_S}^{SW} \\ 0 & w_P \boldsymbol{L}_{V_P} & 0 \\ 0 & 0 & w_S \boldsymbol{L}_{V_S} \\ \lambda_H \boldsymbol{I} & 0 & 0 \\ 0 & \lambda_P \boldsymbol{I} & 0 \\ 0 & 0 & \lambda_S \boldsymbol{I} \end{bmatrix} \begin{bmatrix} \Delta \boldsymbol{H} \\ \Delta \boldsymbol{m}_P \\ \Delta \boldsymbol{m}_S \end{bmatrix} = \begin{bmatrix} \mu_1 \boldsymbol{d}^{T_P} \\ \mu_2 \boldsymbol{d}^{T_S} \\ \mu_3 \boldsymbol{d}^{SW} \\ 0 \\ 0 \\ 0 \\ 0 \\ 0 \end{bmatrix},$$

where $\boldsymbol{G}_H^{T_P}$, $b_H^{T_S}$, $\boldsymbol{G}_{V_P}^{T_P}$, and $\boldsymbol{G}_{V_S}^{T_S}$ are the sensitivity matrices of P- and S-wave arrival times with respect to hypocenter parameters (H), V_P (m_P), and V_S (m_S), respectively; $G_{V_S}^{SW}$ is the sensitivity matrix of surface wave dispersion data with respect to V_S; L_{V_P} and L_{V_S} are the first-order smoothing matrices for V_P and V_S model perturbations with weights of w_P and w_S, respectively; λ_H, λ_P, and λ_S are damping parameters for the hypocenter parameters, V_P, and V_S, respectively; $\Delta \boldsymbol{H}$, $\Delta \boldsymbol{m}_P$, and $\Delta \boldsymbol{m}_S$ are perturbations to the hypocenter parameters and the V_P and V_S models, respectively; $\boldsymbol{d}^{T_P}$, $\boldsymbol{d}^{T_S}$, and $\boldsymbol{d}^{SW}$ are residuals for P- and S-wave arrival times and surface wave dispersion data; and μ_1, μ_2, and μ_3 are data weighting parameters for P-wave arrival times, S-wave arrival times, and surface wave dispersion data, respectively. It is important to select appropriate data weighting parameters for different data types to balance their contributions to the final velocity models.

The damping and smoothing parameters are chosen based on the trade-off analysis between data fitting and model length or smoothness (Hansen, 2000; Zhang HJ et al., 2014). In addition, data weighting parameters are selected based on the trade-off analysis between surface wave data fitting and body wave data fitting so that the final joint inversion velocity models can fit the two types of data equally well (Zhang HJ et al., 2014). The LSQR algorithm (Paige and Saunders, 1982) is used to solve the joint inversion system.

3. Joint Inversion Details and Results

The initial one-dimensional (1D) V_P and V_S models for joint inversion are obtained by averaging the 3D velocity models of Gao YJ et al. (2021b; Figure S7). The grid spacing is defined as 0.2° × 0.5° in the horizontal direction and 10 km in the vertical direction down to a depth of 150 km. Considering significant topographic variations in the study region, we follow the method of Han et al. (2022) to deal with this issue for joint inversion. For the body wave inversion, there is an extra layer above all the stations, and the actual station elevation is considered for calculating ray paths and travel times. For the surface wave inversion, we calculate the dispersion curves based on a series of 1D models. Here, for each surface grid node

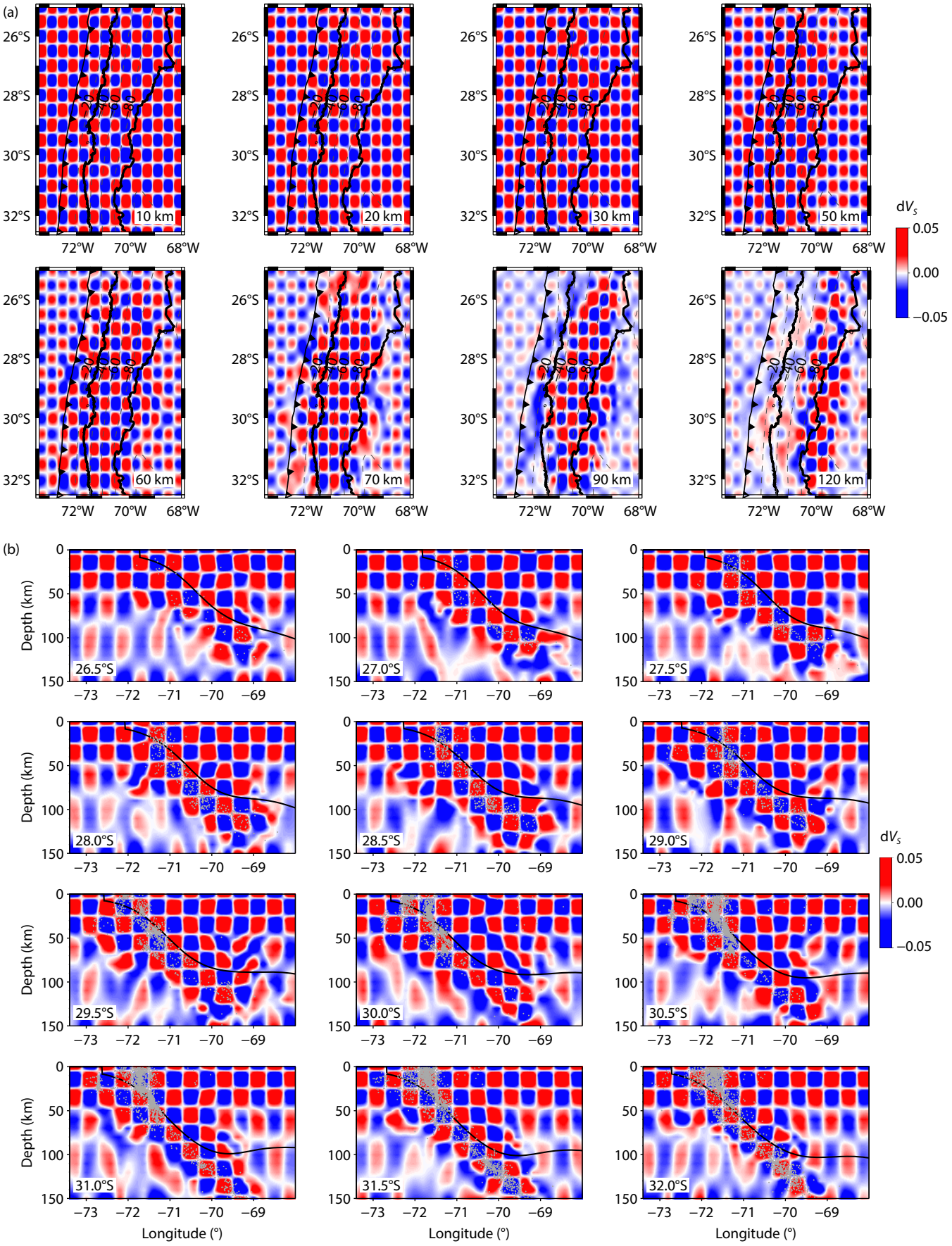

Figure 6. Recovered checkerboard patterns for the V_S model by joint inversion. (a) Depth slices at 10, 20, 30, 50, 60, 70, 90, and 120 km. (b) Vertical sections along different latitudes denoted in the lower left corner of each subplot.

with a surface wave dispersion curve, we construct the 1D model beginning from the free surface based on the actual topography data. In this way, the joint inversion scheme can deal with topographic variations. The optimal damping and smoothing parameters are selected to be 300 and 40 by the trade-off analysis (Hansen, 2000; Figure S8). Similarly, we select the data weighting parameters through a trade-off analysis (Hansen, 2000). Specifically, we first fix the data weighting for body wave data at 1, then vary the data weighting for surface wave data from 1 to 50. From the L-curve produced from the trade-off analysis between the RMS residuals of the body wave data and the surface wave data, we ultimately determine the surface wave weight to be 5 (Figure S8c).

After 12 iterations of joint inversion, the RMS residuals for body wave data and surface wave data decrease to 0.136 s and 0.032 km/s, respectively (Figure S9). As shown in Figure S9, the joint inversion and separate inversions achieve comparable final data residuals. Additionally, the *P*- and *S*-wave arrival time residuals are more concentrated around 0 s compared with the initial models (Figure S10), indicating that the inverted 3D models fit the body wave data better. Furthermore, the fitting between synthetic and observed surface wave dispersion curves at 9 randomly selected grid nodes is good (Figure S11), suggesting the inverted velocity models also fit the surface wave data well.

To evaluate the model resolution, we conduct a checkerboard resolution test (Lévěque et al., 1993). We add ±5% velocity perturbations on adjacent grid nodes in the horizontal directions and on every two grid nodes in the vertical direction of the initial velocity models. The checkerboard models are then used to generate synthetic body wave and surface wave data with the same data distributions as the real data. Gaussian noise with standard deviations of 0.1 s and 0.05 km/s are added to the synthetic body wave data and surface wave data, respectively. Finally, the same inversion strategy as the real data is adopted to recover the checkerboard patterns with the synthetic data. At different depths, the checkerboard patterns for V_S can be recovered well down to 120 km, especially above 70 km (Figure 6). At greater depths (>70 km), although the checkerboard patterns are recovered well, the associated amplitudes are subdued to some extent along both the eastern and western edges of the study region. In contrast, a separate body wave inversion can recover the checkerboard model only in the central region of the study area. As the depth increases, the recoverable region shifts eastward because of the biased distribution of body wave data (Figure S12).

Figure 7 shows different depth slices of the joint inversion V_S model. At depths of 10 and 20 km, relatively high V_S values exist beneath the Coastal Cordillera, bounded to the east by the La Ramada Thrust Belt (Marot et al., 2014). In comparison, distinct low-V_S anomalies appear beneath two volcanic clusters in central Chile, which continue to a depth of 60–70 km. For the southern region with no volcanoes, relatively high V_S values exist at depths

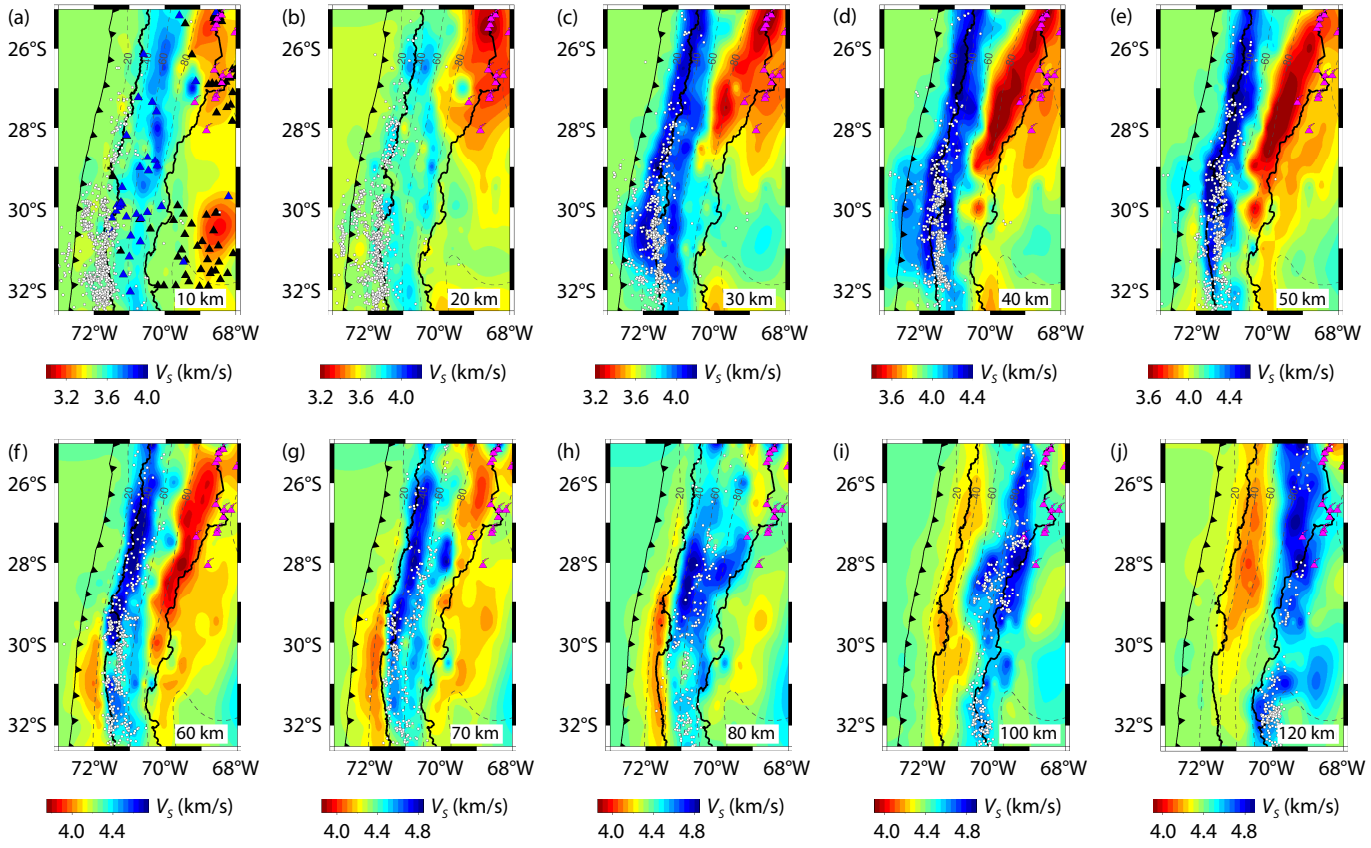

Figure 7. (a–j) The inverted V_S model at depths of 10, 20, 30, 40, 50, 60, 70, 80, 100, and 120 km. The magenta volcanic symbols represent volcanoes, the white dots represent earthquakes within 5 km above and below each depth slice, the blue triangles represent the stations with body wave data, and the black triangles represent the stations with surface wave data.

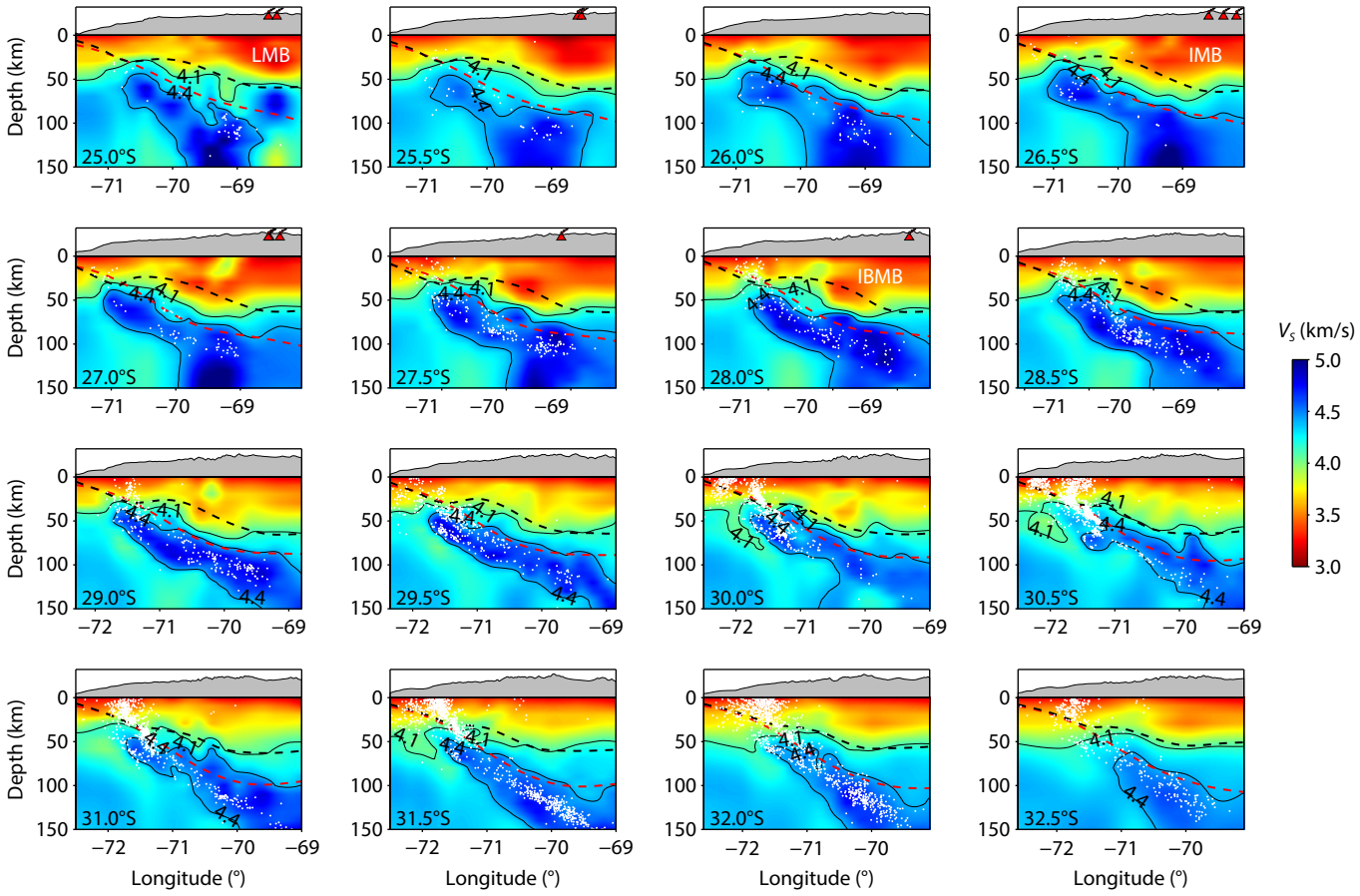

Figure 8. Cross sections of the inverted V_S model along different latitudes. The white dots represent the relocated earthquakes, the dashed black lines mark the continental Moho (Rivadeneyra-Vera et al., 2019), and the dashed red lines mark the slab interface based on the Slab2.0 model (Hayes et al., 2018). LMB, Lazufre Magma Body; IMB, Incahuasi Magma Body; IBMB, Incapillo–Bonete Magma Body.

of 10 and 20 km. Beginning at 30 km, a distinct high-V_S stripe parallel to the trench appears, which shifts eastward with increasing depth. This high-V_S stripe is approximately 100 km wide and seems continuous at depths of 30–50 km, then becomes less continuous and somehow segmented at greater depths. Note that the high-V_S stripe is wider between latitude 26.5°S and 29°S at depths of 80–100 km. Beginning at a depth of 80 km, a parallel low-V_S band is observed to the west of the high-V_S stripe.

The above-mentioned features can also be seen on the cross sections of the V_S model at different latitudes (Figure 8). For example, the high-V_S stripe dipping to the east, which is associated with earthquakes, can clearly be seen. Overall, the upper boundary of this high-V_S band is consistent with the Slab2.0 model to some extent but with some clear differences. From north to south, the seismicity and the pattern of high-velocity anomalies display distinct characteristics. In the northern region (25–27°S), seismicity is relatively sparse, whereas in the southern region, seismicity increases significantly (Figure 1b) and a double seismic zone is observed (Figure 8). In the overriding plate, clear low-V_S anomalies exist beneath volcanoes down to the Moho interface. In comparison, for southern cross sections without volcanoes, no deep low-velocity anomalies exist. Along cross sections, there are also some distinct features. At the latitude of 25°S, a high-velocity blob is imaged above the high-velocity stripe to the east of longitude 69°S. The high-V_S stripe becomes thicker to the east of longitude 70°S and to the north of latitude 28.5°S. To the south of 28.5°S, the high-V_S stripe/band keeps a similar width, and low-V_S anomalies are clear beneath the high-V_S band.

To verify the reliability of the key features in our results, we also conduct a model restoration test (Zhao DP and Hasegawa, 1993). Synthetic body wave arrival times and surface wave dispersion data are generated using the inverted V_S model with the same data distribution as the real data. Similar to the checkerboard resolution test, Gaussian noise with standard deviations of 0.05 km/s for surface wave data and 0.1 s for body wave data is added to simulate their uncertainties, which are then used for joint inversion with the same inversion settings as the real data. The results of the model restoration test indicate that the inverted V_S model closely matches the real model, with the key features effectively recovered, thus demonstrating the reliability of our joint inversion results (Figures S13 and S14).

4. Discussion

4.1 Comparison with Previous Velocity Models in the Region

We compare our joint inversion V_S model with previous models in the same region, including those by Liu M and Gao HY (2022), Gao YJ et al. (2021b), and Gao L et al. (2025), along three profiles at lati-

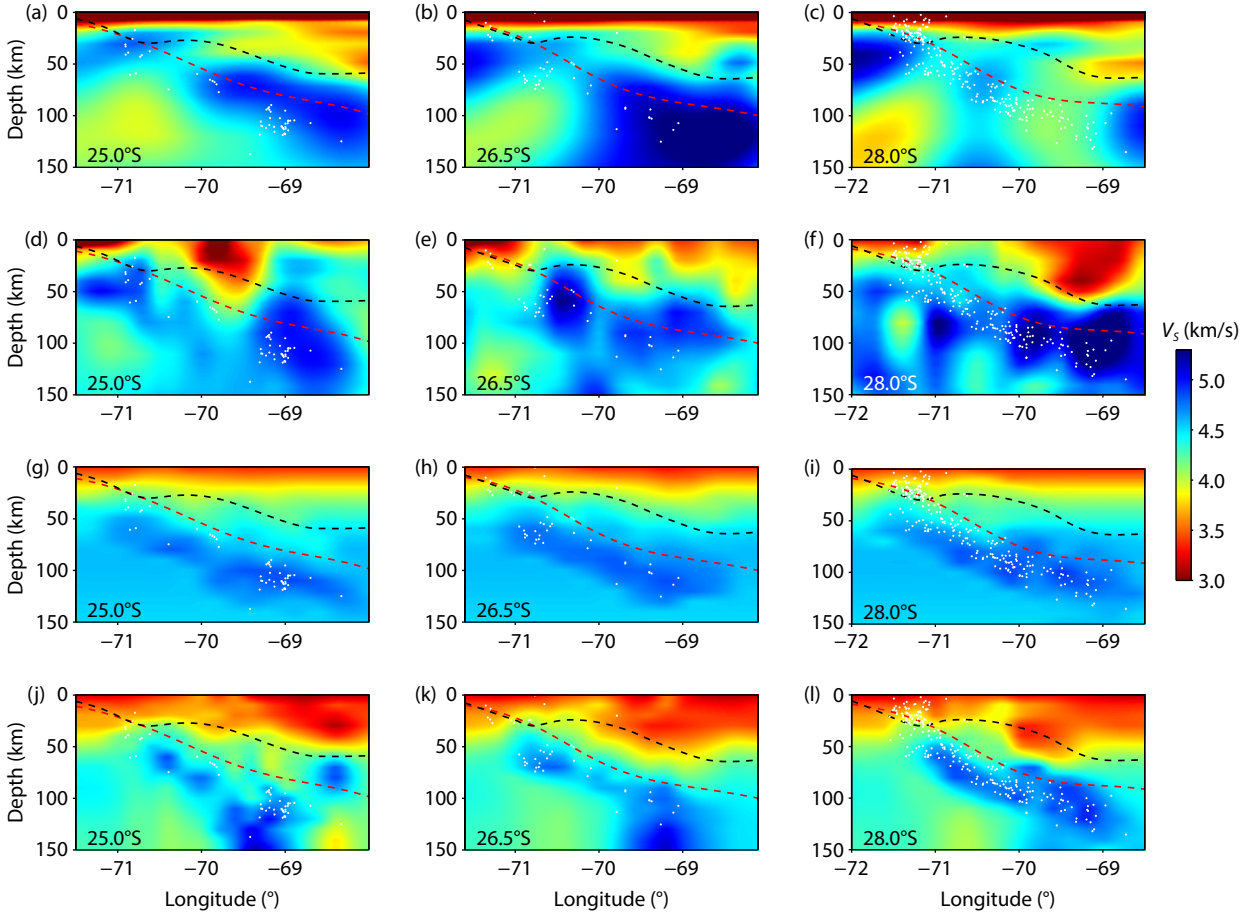

Figure 9. Cross sections through different V_S models along 25°S, 26.5°S, and 28°S. The white dots represent the relocated earthquakes, the dashed black lines mark the continental Moho (Rivadeneyra-Vera et al., 2019), and the dashed red lines mark the slab interface based on the Slab2.0 model. (a–c) Velocity model by Liu M and Gao HY (2022). (d–f) Velocity model by Gao YJ et al. (2021b). (g–i) Velocity model by Gao L et al. (2025). (j–l) Velocity model from this study.

tudes of 25°S, 26.5°S, and 28°S (Figure 9). In general, all the studies reveal eastward-dipping high-velocity anomalies along different profiles, which should represent the subducting Nazca Plate. However, the different models clearly show different velocity features. The model by Liu M and Gao HY (2022) shows discontinuous high-velocity anomalies and lacks an evident slab-like high-velocity band, such as in the section at 28°S (Figure 9c). This occurs because the model is determined only by surface wave data, which have limited resolutions at depth. In comparison, the V_S model by Gao YJ et al. (2021b), which is determined from full waveform inversion, shows clearer eastward-dipping high-V_S anomalies. However, the upper boundary of high-V_S anomalies is more consistent with the Moho interface than the Slab2.0 model. Some spurious low-velocity anomalies also occur within the high-velocity band representative of the subducting slab. For the model by Gao L et al. (2025), which is determined by the DD seismic tomography method using only body wave arrival times, the slab-like high-V_S anomalies are better imaged than in the models by Liu M and Gao HY (2022) and Gao YJ et al. (2021b). This is because the DD tomography method has the ability to better resolve the velocity structure in the source region. However, because of the ray coverage limitation between the intraslab seismicity and regional seismic stations, the zone beneath the slab is not well resolved.

In comparison, our joint inversion V_S model not only well resolves dipping high-velocity anomalies associated with the subducting slab, but also resolves low-velocity anomalies beneath the slab. This is evident in the comparison of recovered checkerboard patterns by Gao L et al. (2025) and our joint inversion (Figure S12). Furthermore, low velocities in the continental crust beneath volcanoes are better resolved by joint inversion compared with the model by Gao L et al. (2025). This is because the incorporation of short-period surface waves can help with imaging the shallow structures, as shown in the surface wave-only inversion model by Liu M and Gao HY (2022; Figure 9).

4.2 Velocity Features Within and Beneath the Slab

The primary feature in the V_S model is the eastward-dipping high-velocity anomalies enclosed by the contour of 4.4 km/s, which correspond to the subducting Nazca Plate. Overall, the high-velocity anomalies are associated with the relocated earthquakes, and their upper boundaries in different cross sections are consistent with the slab interfaces from the Slab2.0 model (Figure 8). Above ~100 km, the high-velocity anomaly band exhibits a width of approximately 40–50 km. On the basis of the relationship

between the age and thermal gradient of the Nazca Plate (Stein and Stein, 1992; Müller et al., 2008) and receiver function imaging (Sodoudi et al., 2011), the thickness of the Nazca Plate is estimated to be approximately 50 km (Ji YF et al., 2019). Compared with the other velocity models by Liu M and Gao HY (2022) and Gao YJ et al. (2021b), our joint inversion V_S model is more consistent with the slab thickness estimation. Note that between 25°S and 28.5°S in latitude, high-velocity anomalies are present beneath the normal slab to the east of longitude 70°W, which makes the slab seem thicker. The cause of this local feature requires further investigation.

To the south of 27°S, the intraslab seismicity spreads over almost the entire slab above a depth of ~100 km, whereas north of 27°S, seismic activity is relatively low, particularly around 26.5°S, where a seismic gap is known to exist (Isacks, 1988; Cahill and Isacks, 1992). This gap could be caused by the slab tearing as a result of the transition from normal subduction in the north to flat slab subduction in the south (Gao L et al., 2025). In contrast to northern Chile, where a prominent double seismic zone exists (Rietbrock and Waldhauser, 2004; Comte et al., 2016; Sippl et al., 2018), in the central Chile flat slab region, it is less pronounced and observed only south of 29.5°S (Figure 8), with a separation of approximately 20 km between the upper and lower planes. The upper seismicity plane generally corresponds to the phase transition from lawsonite–blueschist to lawsonite–eclogite within the subducting oceanic crust (Hacker et al., 2003), which has high-V_S values. The lower seismicity plane is typically associated with dehydration of serpentinite (Peacock, 2001), where supercritical fluids could exist because of higher pressures and temperatures (Chen TN et al., 2024) and result in higher V_S. This assumption is also consistent with low V_P/V_S values associated with the lower seismicity plane (Gao L et al., 2025). One notable feature is a high-velocity anomaly imaged near 25°S, located between the Moho and the upper interface of the subducting plate (Figure 8). This anomaly may correspond to the delaminated block from the North Puna Plateau (Schurr et al., 2006; Bianchi et al., 2013; Gao YJ et al., 2021a).

Furthermore, low-velocity anomalies are imaged beneath the high-velocity slab, which is also identified in the model by Liu M and Gao HY (2022; Figure 9). Although the V_S model resolution is slightly worse below the slab, the checkerboard patterns can still be resolved to some extent (Figure 6). In addition, the model restoration test shows that the low-velocity anomalies below the slab can be recovered (Figure S14). These tests suggest that the imaged low-velocity anomalies below the slab are robust. A similar phenomenon was previously observed for the Cascadia subduction zone, where low-velocity anomalies were imaged directly beneath the Juan de Fuca slab (Hawley et al., 2016). Some studies have suggested that the low-velocity anomalies can be attributed to anisotropy (Tauzin et al., 2016). However, it is more widely accepted that they are likely associated with the accumulation of melts directly below the slab, which should have low viscosity. This low-viscosity layer beneath the slab was found to be necessary to fit for the postseismic displacement of the 2012 Indian Ocean earthquake (Hu Y et al., 2016). Comparable observations have also been made for the Cocos Plate, where the subducting slab may be weakened by the presence of low-velocity, low-viscosity materials beneath it (Liu M and Gao HY, 2023).

Naif et al. (2013) further revealed through magnetotelluric data a partially melted channel less than 30 km thick along the lithosphere–asthenosphere boundary of the Cocos Plate, which may act as a lubricant for the plate movement. In addition, the receiver function imaging confirms the presence of a low-velocity layer beneath the subducting slab (Wang X et al., 2024). Therefore, our study, combined with other studies, provides further evidence that the low-velocity layer existing below the slab could be a global phenomenon.

Along some cross sections, the seismicity distribution does not match the upper boundary of the 4.4 km/s high-velocity contour, especially at 28.0°S and 31.0°S (Figure 8). This inconsistency was noticed by Gao L et al. (2025), who interpreted high-velocity anomalies above the intraslab seismicity as the subducted aseismic seamounts. Our joint inversion V_S model better illustrates this phenomenon along cross sections at 28°S and 31.0°S, which coincide with the predicted paths of the Copiapó Ridge and the JFR. Similar to Gao L et al. (2025), our joint inversion V_S model provides direct seismic evidence of the subducted aseismic ridge, which is the main reason the slab becomes flat from normal subduction.

4.3 Low-Velocity Anomalies in the Crust Beneath Volcanoes

In our model, the 4.1 km/s contour corresponds closely to the Moho interface, showing the significant thickening of the continental crust beneath the Andes, as previously revealed by receiver function, gravity, and geodynamic studies (Tassara and Echaurren, 2012; Rivadeneyra-Vera et al., 2019). In the continental crust to the north of 28°S, our joint inversion V_S model reveals widespread low-velocity anomalies, which are deeper and lower in the east than in the west. To the north of 28°S lies the Central Volcanic Zone (CVZ) in the central Andes, characterized by widespread arc volcanism. Therefore, our results align with previous observations (Ward et al., 2017; Gao YJ et al., 2021a) and reveal significant low-velocity anomalies beneath the volcanic arcs, especially at 25°S, 26.5°S, and 28°S, corresponding to the Lazufre Magma Body (LMB), Incahuasi Magma Body (IMB), and Incapillo–Bonete Magma Body (IBMB), respectively. For the northern part of the CVZ, the low-velocity anomalies are most likely attributed to magmas in the crust, which are fed by partial melting in the mantle wedge that is due to released fluids from dehydration reactions in the slab. This assumption is supported by the widespread presence of high V_P/V_S values in the mantle wedge below the CVZ in this region (Leon-Rios et al., 2024; Gao L et al., 2025). However, for the southern part of the CVZ, the volcanoes are more likely caused by slab tearing when the slab transits from normal subduction to flat subduction (Gao L et al., 2025). The upwelling hot mantle materials can move through the slab tear and enter the crust to form magma chambers for various volcanoes.

Moreover, the low-velocity anomalies in the crust almost disappear to the south of 28°S, indicating the lack of magma bodies in the crust. This finding is consistent with the volcanic gap between the CVZ and the Southern Volcanic Zone (SVZ) from ~28°S to 33°S, which corresponds well with the flat slab subduction region

(Barazangi and Isacks, 1976).

5. Conclusions

In this study, we have assembled body wave arrival times and constructed surface wave phase velocity maps in central Chile, which are used for joint inversion of the subduction zone velocity structure. Compared with other velocity models in the region that are determined by the individual data type, our joint inversion V_S model shows better consistency with the intraslab seismicity distribution as well as the Moho and slab interfaces. Our V_S model clearly images an eastward-dipping high-velocity band of 40–50 km thick, corresponding well with the thickness of the Nazca Plate estimated by thermal modeling. As in some subduction zones, we also image a low-velocity layer beneath the subducting plate, which may be due to partial melting. Along the subduction paths of the Copiapó Ridge and the JFR, our joint inversion V_S model clearly shows high-velocity bodies above the intraslab seismicity, which are likely associated with subducted seamounts. Additionally, our joint inversion V_S model shows widespread low-velocity anomalies in the crust beneath the CVZ, indicating the existence of magma bodies beneath the volcanic arc. Overall, the joint inversion of body wave arrival times and surface wave phase velocity maps takes advantage of the complementary strengths of each data type and better resolves the central Chile subduction zone.

Acknowledgments

We are grateful to Meng Liu and Haiying Gao for providing the empirical Green's functions from ambient noise data in Chile. This research was funded by the National Natural Science Foundation of China under Grant 42230101, the National Agency for Research and Development of Chile (ANID) by Projects AFB180004 and AFB220002, and the ANID Programa de Cooperación Internacional (PCI) Grant PII-180003.

References

Angermann, D., Klotz, J., and Reigber, C. (1999). Space–geodetic estimation of the Nazca–South America Euler vector. *Earth Planet. Sci. Lett.*, *171*(3), 329–334. https://doi.org/10.1016/S0012-821X(99)00173-9

Barazangi, M., and Isacks, B. L. (1976). Spatial distribution of earthquakes and subduction of the Nazca plate beneath South America. *Geology*, *4*(11), 686–692. https://doi.org/10.1130/0091-7613(1976)4<686:SDOEAS>2.0.CO;2

Bello-González, J. P., Contreras-Reyes, E., and Arriagada, C. (2018). Predicted path for hotspot tracks off South America since Paleocene times: Tectonic implications of ridge–trench collision along the Andean margin. *Gondwana Res.*, *64*, 216–234. https://doi.org/10.1016/j.gr.2018.07.008

Bianchi, M., Heit, B., Jakovlev, A., Yuan, X., Kay, S. M., Sandvol, E., Alonso, R. N., Coira, B., Brown, L., Kind, R., and Comte, D. (2013). Teleseismic tomography of the southern Puna plateau in Argentina and adjacent regions. *Tectonophysics*, *586*, 65–83. https://doi.org/10.1016/j.tecto.2012.11.016

Cahill, T., and Isacks, B. L. (1992). Seismicity and shape of the subducted Nazca Plate. *J. Geophys. Res.: Solid Earth*, *97*(B12), 17503–17529. https://doi.org/10.1029/92JB00493

Chen, T. N., Chen, R. X., Zheng, Y. F., Zhou, K., and Li, W. C. (2024). Subduction zone rocks oxidized by supercritical fluid: Constraints from an ultrahigh-pressure eclogite-vein system in the Dabie orogen, China. *Geol. Soc. Am. Bull.* 137(5–6), 2358–2374. https://doi.org/10.1130/B37979.1

Comte, D., Carrizo, D., Roecker, S., Ortega-Culaciati, F., and Peyrat, S. (2016). Three-dimensional elastic wave speeds in the northern Chile subduction zone: Variations in hydration in the supraslab mantle. *Geophys. J. Int.*, *207*(2), 1080–1105. https://doi.org/10.1093/gji/ggw318

Contreras-Reyes, E., and Carrizo, D. (2011). Control of high oceanic features and subduction channel on earthquake ruptures along the Chile–Peru subduction zone. *Phys. Earth Planet. Inter.*, *186*(1-2), 49–58. https://doi.org/10.1016/j.pepi.2011.03.002

Cross, T. A., and Pilger, R. H. Jr. (1982). Controls of subduction geometry, location of magmatic arcs, and tectonics of arc and back-arc regions. *Geol. Soc. Am. Bull.*, *93*(6), 545–562. https://doi.org/10.1130/0016-7606(1982)93<545:COSGLO>2.0.CO;2

DeMets, C., Gordon, R. G., and Argus, D. F. (2010). Geologically current plate motions. *Geophys. J. Int.*, *181*(1), 1–80. https://doi.org/10.1111/j.1365-246X.2009.04491.x

Fang, H. J., Zhang, H. J., Yao, H. J., Allam, A., Zigone, D., Ben-Zion, Y., Clifford Thurber and van der Hilst, R. D. (2016). A new algorithm for three-dimensional joint inversion of body wave and surface wave data and its application to the Southern California plate boundary region. *Journal of Geophysical Research: Solid Earth*, *121*(5), 3557–3569. https://doi.org/10.1002/2015JB012702

Gans, C. R., Beck, S. L., Zandt, G., Gilbert, H., Alvarado, P., Anderson, M., and Linkimer, L. (2011). Continental and oceanic crustal structure of the Pampean flat slab region, western Argentina, using receiver function analysis: New high-resolution results. *Geophys. J. Int.*, *186*(1), 45–58. https://doi.org/10.1111/j.1365-246X.2011.05023.x

Gao, L., Chen, Z. X., Liu, Y., Zhang, H. J., Hu, J. S., Comte, D., and Culaciati, F. H. O. (2025). High-resolution seismic tomography of the transition zone from normal to flat slab subduction in central Chile: Implications for volcanoes, plate coupling and flat subduction. *Earth Planet. Sci. Lett.*, *651*, 119167. https://doi.org/10.1016/j.epsl.2024.119167

Gao, Y. J., Tilmann, F., van Herwaarden, D. P., Thrastarson, S., Fichtner, A., Heit, B., Yuan, X. H., and Schurr, B. (2021a). Full waveform inversion beneath the central Andes: Insight into the dehydration of the Nazca slab and delamination of the back-arc lithosphere. *J. Geophys. Res.: Solid Earth*, *126*(7), e2021JB021984. https://doi.org/10.1029/2021JB021984

Gao, Y. J., Yuan, X. H., Heit, B., Tilmann, F., van Herwaarden, D. P., Thrastarson, S., Fichtner, A., and Schurr, B. (2021b). Impact of the Juan Fernandez ridge on the Pampean flat subduction inferred from full waveform inversion. *Geophys. Res. Lett.*, *48*(21), e2021GL095509. https://doi.org/10.1029/2021GL095509

Golos, E. M., Fang, H., Yao, H., Zhang, H., Burdick, S., Vernon, F., Schaeffer, A., Lebedev, S., and van der Hilst, R. D. (2018). Shear wave tomography beneath the United States using a joint inversion of surface and body waves. *J. Geophys. Res.: Solid Earth*, *123*(6), 5169–5189. https://doi.org/10.1029/2017JB014894

Gutscher, M. A., Spakman, W., Bijwaard, H., and Engdahl, E. R. (2000). Geodynamics of flat subduction: Seismicity and tomographic constraints from the Andean margin. *Tectonics*, *19*(5), 814–833. https://doi.org/10.1029/1999TC001152

Hacker, B. R., Peacock, S. M., Abers, G. A., and Holloway, S. D. (2003). Subduction factory 2. Are intermediate-depth earthquakes in subducting slabs linked to metamorphic dehydration reactions?. *J. Geophys. Res.: Solid Earth*, *108*(B1), 2030. https://doi.org/10.1029/2001JB001129

Haddon, A., and Porter, R. (2018). *S*-wave receiver function analysis of the Pampean flat-slab region: Evidence for a torn slab. *Geochem. Geophys. Geosyst.*, *19*(10), 4021–4034. https://doi.org/10.1029/2018GC007868

Han, S. C., Zhang, H. J., Xin, H. L., Shen, W. S., and Yao, H. J. (2022). USTClitho2.0: Updated unified seismic tomography models for Continental China lithosphere from joint inversion of body-wave arrival times and surface-wave dispersion data. *Seismol. Res. Lett.*, *93*(1), 201–215. https://doi.org/10.1785/0220210122

Hansen, P. C. (2000). The L-curve and its use in the numerical treatment of inverse problems. Computational Inverse Problems in Electrocardiology. WIT Press, pp. 119–142.

Hawley, W. B., Allen, R. M., and Richards, M. A. (2016). Tomography reveals buoyant asthenosphere accumulating beneath the Juan de Fuca plate.

Science, *353*(6306), 1406–1408. https://doi.org/10.1126/science.aad8104

Hayes, G. P., Moore, G. L., Portner, D. E., Hearne, M., Flamme, H., Furtney, M., and Smoczyk, G. M. (2018). Slab2, a comprehensive subduction zone geometry model. *Science*, *362*(6410), 58–61. https://doi.org/10.1126/science.aat4723

Hu, Y., Bürgmann, R., Banerjee, P., Feng, L. J., Hill, E. M., Ito, T., Tabei, T., and Wang, K. L. (2016). Asthenosphere rheology inferred from observations of the 2012 Indian Ocean earthquake. *Nature*, *538*(7625), 368–372. https://doi.org/10.1038/nature19787

Isacks, B. L. (1988). Uplift of the Central Andean Plateau and bending of the Bolivian Orocline. *J. Geophys. Res.: Solid Earth*, *93*(B4), 3211–3231. https://doi.org/10.1029/JB093iB04p03211

Ji, Y. F., Yoshioka, S., Manea, V. C., Manea, M., and Suenaga, N. (2019). Subduction thermal structure, metamorphism and seismicity beneath north-central Chile. *J. Geodyn.*, *129*, 299–312. https://doi.org/10.1016/j.jog.2018.09.004

Kopp, H., Flueh, E. R., Papenberg, C., and Klaeschen, D. (2004). Seismic investigations of the O'Higgins Seamount Group and Juan Fernández Ridge: Aseismic ridge emplacement and lithosphere hydration. *Tectonics*, *23*(2), TC2009. https://doi.org/10.1029/2003TC001590

Leon-Rios, S., Reyes-Wagner, V., Calle-Gardella, D., Rietbrock, A., Roecker, S., Maksymowicz, A., and Comte, D. (2024). Structural characterization of the Taltal segment in northern Chile between 22°S and 26°S using local earthquake tomography. *Geochem. Geophys. Geosyst.*, *25*(5), e2023GC011197. https://doi.org/10.1029/2023GC011197

Lévěque, J. J., Rivera, L., and Wittlinger, G. (1993). On the use of the checker-board test to assess the resolution of tomographic inversions. *Geophys. J. Int.*, *115*(1), 313–318. https://doi.org/10.1111/j.1365-246X.1993.tb05605.x

Liu, M., and Gao, H. Y. (2022). Three-dimensional variation of the slab geometry within the South American subduction system. *Geophys. Res. Lett.*, *49*(2), e2021GL095924. https://doi.org/10.1029/2021GL095924

Liu, M., and Gao, H. Y. (2023). Role of subduction dynamics on the unevenly distributed volcanism at the Middle American subduction system. *Sci. Rep.*, *13*(1), 14697. https://doi.org/10.1038/s41598-023-41740-y

Lomax, A., Virieux, J., Volant, P., and Berge-Thierry, C. (2000). Probabilistic earthquake location in 3D and layered models: Introduction of a Metropolis–Gibbs method and comparison with linear locations. In C. H. Thurber, et al. (Eds.), *Advances in Seismic Event Location* (pp. 101–134), Dordrecht: Springer. https://doi.org/10.1007/978-94-015-9536-0_5

Maceira, M., and Ammon, C. J. (2009). Joint inversion of surface wave velocity and gravity observations and its application to central Asian basins shear velocity structure. *J. Geophys. Res.: Solid Earth*, *114*(B2), B02314. https://doi.org/10.1029/2007JB005157

Manea, V. C., Pérez-Gussinyé, M., and Manea, M. (2012). Chilean flat slab subduction controlled by overriding plate thickness and trench rollback. *Geology*, *40*(1), 35–38. https://doi.org/10.1130/G32543.1

Marot, M., Monfret, T., Gerbault, M., Nolet, G., Ranalli, G., and Pardo, M. (2014). Flat versus normal subduction zones: A comparison based on 3-D regional traveltime tomography and petrological modelling of central Chile and western Argentina (29°–35°S). *Geophys. J. Int.*, *199*(3), 1633–1654. https://doi.org/10.1093/gji/ggu355

Müller, R. D., Sdrolias, M., Gaina, C., Steinberger, B., and Heine, C. (2008). Long-term sea-level fluctuations driven by ocean basin dynamics. *Science*, *319*(5868), 1357–1362. https://doi.org/10.1126/science.1151540

Naif, S., Key, K., Constable, S., and Evans, R. L. (2013). Melt-rich channel observed at the lithosphere–asthenosphere boundary. *Nature*, *495*(7441), 356–359. https://doi.org/10.1038/nature11939

Navarro-Aránguiz, A., Comte, D., Farías, M., Roecker, S., Calle-Gardella, D., Zhang, H. J., Gao, L., and Rietbrock, A. (2022). Subduction erosion and basal accretion in the Central Chile subduction wedge inferred from local earthquake tomography. *J. South Am. Earth Sci.*, *115*, 103765. https://doi.org/10.1016/j.jsames.2022.103765

O'Driscoll, L. J., Richards, M. A., and Humphreys, E. D. (2012). Nazca–South America interactions and the late Eocene–late Oligocene flat-slab episode in the central Andes. *Tectonics*, *31*(2), TC2013. https://doi.org/10.1029/2011TC003036

Paige, C. C., and Saunders, M. A. (1982). LSQR: An algorithm for sparse linear equations and sparse least squares. *ACM Trans. Math. Softw.*, *8*(1), 43–71. https://doi.org/10.1145/355984.355989

Peacock, S. M. (2001). Are the lower planes of double seismic zones caused by serpentine dehydration in subducting oceanic mantle?. *Geology*, *29*(4), 299–302. https://doi.org/10.1130/0091-7613(2001)029<0299:ATLPOD>2.0.CO;2

Pilger, R. H. (1981). Plate reconstructions, aseismic ridges, and low-angle subduction beneath the Andes. *Geol. Soc. Am. Bull.*, *92*(7), 448–456. https://doi.org/10.1130/0016-7606(1981)92<448:PRARAL>2.0.CO;2

Portner, D. E., Beck, S., Zandt, G., and Scire, A. (2017). The nature of subslab slow velocity anomalies beneath South America. *Geophys. Res. Lett.*, *44*(10), 4747–4755. https://doi.org/10.1002/2017GL073106

Portner, D. E., Rodríguez, E. E., Beck, S., Zandt, G., Scire, A., Rocha, M. P., Bianchi, M. B., Ruiz, M., França, G. S., … Alvarado, P. (2020). Detailed structure of the subducted Nazca slab into the lower mantle derived from continent-scale teleseismic *P* wave tomography. *J. Geophys. Res.: Solid Earth*, *125*(5), e2019JB017884. https://doi.org/10.1029/2019JB017884

Ramos, V. A., and Folguera, A. (2009). Andean flat-slab subduction through time. *Geol. Soc. London Spec. Publ.*, *327*(1), 31–54. https://doi.org/10.1144/SP327.3

Rawlinson, N., and Sambridge, M. (2003). Seismic traveltime tomography of the crust and lithosphere. *Adv. Geophys.*, *46*, 81–198. https://doi.org/10.1016/S0065-2687(03)46002-0

Rawlinson, N., and Sambridge, M. (2005). The fast marching method: An effective tool for tomographic imaging and tracking multiple phases in complex layered media. *Explor. Geophys.*, *36*(4), 341–350. https://doi.org/10.1071/EG05341

Rietbrock, A., and Waldhauser, F. (2004). A narrowly spaced double-seismic zone in the subducting Nazca plate. *Geophys. Res. Lett.*, *31*(10), L10608. https://doi.org/10.1029/2004GL019610

Rivadeneyra-Vera, C., Bianchi, M., Assumpção, M., Cedraz, V., Julià, J., Rodríguez, M., Sánchez, L., Sánchez, G., Lopez-Murua, L., … The "3-Basins" Project Team. (2019). An updated crustal thickness map of central South America based on receiver function measurements in the region of the Chaco, Pantanal, and Paraná Basins, southwestern Brazil. *J. Geophys. Res.: Solid Earth*, *124*(8), 8491–8505. https://doi.org/10.1029/2018JB016811

Saito, M. (1988). DISPER80: A subroutine package for calculation of seismic normal-mode solutions. In D. J. Doornbos (Ed.), *Seismological Algorithms: Computational Methods and Computer Programs* (pp. 293–319). San Diego, California: Academic Press.

Schurr, B., Rietbrock, A., Asch, G., Kind, R., and Oncken, O. (2006). Evidence for lithospheric detachment in the central Andes from local earthquake tomography. *Tectonophysics*, *415*(1-4), 203–223. https://doi.org/10.1016/j.tecto.2005.12.007

Sippl, C., Schurr, B., Asch, G., and Kummerow, J. (2018). Seismicity structure of the northern Chile forearc from >100,000 double-difference relocated hypocenters. *J. Geophys. Res.: Solid Earth*, *123*(5), 4063–4087. https://doi.org/10.1002/2017JB015384

Sodoudi, F., Yuan, X., Asch, G., and Kind, R. (2011). High-resolution image of the geometry and thickness of the subducting Nazca lithosphere beneath northern Chile. *J. Geophys. Res.: Solid Earth*, *116*(B4), B04302. https://doi.org/10.1029/2010JB007829

Stein, C. A., and Stein, S. (1992). A model for the global variation in oceanic depth and heat flow with lithospheric age. *Nature*, *359*(6391), 123–129. https://doi.org/10.1038/359123a0

Syracuse, E. M., Maceira, M., Prieto, G. A., Zhang, H. J., and Ammon, C. J. (2016). Multiple plates subducting beneath Colombia, as illuminated by seismicity and velocity from the joint inversion of seismic and gravity data. *Earth Planet. Sci. Lett.*, *444*, 139–149. https://doi.org/10.1016/j.epsl.2016.03.050

Syracuse, E. M., Zhang, H., and Maceira, M. (2017). Joint inversion of seismic and gravity data for imaging seismic velocity structure of the crust and upper mantle beneath Utah, United States. *Tectonophysics*, *718*, 105–117. https://doi.org/10.1016/j.tecto.2017.07.005

Tassara, A., and Echaurren, A. (2012). Anatomy of the Andean subduction zone: Three-dimensional density model upgraded and compared against global-scale models. *Geophys. J. Int.*, *189*(1), 161–168. https://doi.org/10.1111/j.

1365-246X.2012.05397.x

Tauzin, B., Bodin, T., Debayle, E., Perrillat, J. P., and Reynard, B. (2016). Multi-mode conversion imaging of the subducted Gorda and Juan de Fuca plates below the North American continent. *Earth Planet. Sci. Lett.*, *440*, 135–146. https://doi.org/10.1016/j.epsl.2016.01.036

von Huene, R., Corvalán, J., Flueh, E. R., Hinz, K., Korstgard, J., Ranero, C. R., and Weinrebe, W. (1997). Tectonic control of the subducting Juan Fernández Ridge on the Andean margin near Valparaiso, Chile. *Tectonics*, *16*(3), 474–488. https://doi.org/10.1029/96tc03703

Wagner, L. S., Beck, S., and Zandt, G. (2005). Upper mantle structure in the south central Chilean subduction zone (30° to 36°S). *J. Geophys. Res.: Solid Earth*, *110*(B1), B01308. https://doi.org/10.1029/2004JB003238

Wagner, L. S., Beck, S., Zandt, G., and Ducea, M. N. (2006). Depleted lithosphere, cold, trapped asthenosphere, and frozen melt puddles above the flat slab in central Chile and Argentina. *Earth Planet. Sci. Lett.*, *245*(1-2), 289–301. https://doi.org/10.1016/j.epsl.2006.02.014

Wang, X., Chen, L., Wang, K. L., Chen, Q. F., Zhan, Z. W., and Yang, J. F. (2024). Seismic evidence for melt-rich lithosphere–asthenosphere boundary beneath young slab at Cascadia. *Nat. Commun.*, *15*(1), 3504. https://doi.org/10.1038/s41467-024-47887-0

Ward, K. M., Porter, R. C., Zandt, G., Beck, S. L., Wagner, L. S., Minaya, E., and Tavera, H. (2013). Ambient noise tomography across the Central Andes. *Geophys. J. Int.*, *194*(3), 1559–1573. https://doi.org/10.1093/gji/ggt166

Ward, K. M., Delph, J. R., Zandt, G., Beck, S. L., and Ducea, M. N. (2017). Magmatic evolution of a Cordilleran flare-up and its role in the creation of silicic crust. *Sci. Rep.*, *7*(1), 9047. https://doi.org/10.1038/s41598-017-09015-5

Yáñez, G. A., Ranero, C. R., von Huene, R., and Díaz, J. (2001). Magnetic anomaly interpretation across the southern central Andes (32°–34°S): The role of the Juan Fernández Ridge in the late Tertiary evolution of the margin. *J. Geophys. Res.: Solid Earth*, *106*(B4), 6325–6345. https://doi.org/10.1029/2000JB900337

Yang, S. B., Zhang, H. J., Gu, N., Gao, J., Xu, J., Jin, J. Q., Li, J. L., and Yao, H. J. (2022). Automatically extracting surface-wave group and phase velocity dispersion curves from dispersion spectrograms using a convolutional neural network. *Seismol. Res. Lett.*, *93*(3), 1549–1563. https://doi.org/10.1785/0220210280

Zhang, H. J. and Thurber, C. (2003). Double-Difference Tomography: The Method and Its Application to the Hayward Fault, California. *Bulletin of the Seismological Society of America*, 93(5), 1875–1889. https://doi.org/10.1785/0120020190

Zhang, H. J., Roecker, S., Thurber, C. H., and Wang, W. J. (2012). Seismic imaging of microblocks and weak zones in the crust beneath the southeastern margin of the Tibetan Plateau. In I. A. Dar (Ed.), *Earth Sciences* (pp. 159–202). Rijeka: IntechOpen. https://doi.org/10.5772/27876

Zhang, H. J., Maceira, M., Roux, P., and Thurber, C. (2014). Joint inversion of body-wave arrival times and surface-wave dispersion for three-dimensional seismic structure around SAFOD. *Pure Appl. Geophys.*, *171*(11), 3013–3022. https://doi.org/10.1007/s00024-014-0806-y

Zhao, D. P., and Hasegawa, A. (1993). *P* wave tomographic imaging of the crust and upper mantle beneath the Japan Islands. *J. Geophys. Res.: Solid Earth*, *98*(B3), 4333–4353. https://doi.org/10.1029/92JB02295